Imp2p forms actin-dependent clusters and imparts stiffness to the contractile ring

Kimberly Bellingham-Johnstun†, Blake Commer†, Brié Levesque, Zoe L. Tyree, and Caroline Laplante*
Department of Molecular Biomedical Sciences, North Carolina State University, Raleigh, NC 27607

ABSTRACT **The contractile ring must anchor to the plasma membrane and cell wall to transmit its tension. F-BAR domain containing proteins including Imp2p and Cdc15p in fission yeast are likely candidate anchoring proteins based on their mutant phenotypes. Cdc15p is a node component, links the actin bundle to the plasma membrane, recruits Bgs1p to the division plane, prevents contractile ring sliding, and contributes to the stiffness of the contractile ring. Less is known about Imp2p. We found that similarly to Cdc15p, Imp2p contributes to the stiffness of the contractile ring and assembles into protein clusters. Imp2p clusters contain approximately eight Imp2p dimers and depend on the actin network for their stability at the division plane. Importantly, Imp2p and Cdc15p reciprocally affect the amount of each other in the contractile ring, indicating that the two proteins influence each other during cytokinesis, which may partially explain their similar phenotypes.**

Monitoring Editor
Laurent Blanchoin
CEA Grenoble

Received: Jun 23, 2022
Revised: Oct 13, 2022
Accepted: Oct 18, 2022

INTRODUCTION

The mechanism that anchors the contractile ring to the plasma membrane and the extracellular matrix is critical for generating the tension that drives cytokinesis. Although the exact molecular composition of this mechanism remains unclear, the Fer/CIP4 homology Bin-Amphiphysin-Rvs (F-BAR) domain containing proteins Cdc15p and Imp2p are strong candidates for this mechanism in fission yeast. Previous studies have shown that cells mutant for *cdc15* or depleted of Cdc15p and cells with mutations in *imp2* exhibit a contractile ring sliding phenotype (Arasada and Pollard, 2014; Martin-Garcia *et al.*, 2014; McDonald *et al.*, 2015; Snider *et al.*, 2017, 2020; Willet *et al.*, 2021). In those cells, the ring slides away from where it assembled before the onset of constriction, resulting in asymmetric cell division. In fission yeast, a contractile ring sliding off the division plane during cytokinesis is a hallmark phenotype of defective anchoring of the contractile ring. Presumably, poor anchoring of the contractile ring results in its displacement along the cell length when the ring is experiencing sufficient tension (Arasada and Pollard, 2014). Poor anchoring of the contractile ring and therefore transmission of tension would also result in a decreased constriction rate, which has been measured previously in cells with defective Cdc15p or Imp2p (Willet *et al.*, 2021; Moshtohry *et al.*, 2022).

More is known about the role of Cdc15p as a putative protein anchor than about Imp2p. There are two possible and non–mutually exclusive explanations for the sliding of the contractile ring in Cdc15p deficient cells. The first explanation is that Cdc15p itself may anchor the contractile ring to the plasma membrane by interacting directly with the plasma membrane and indirectly with the actin cytoskeleton via binding of Cdc12p and Myo2 molecules (composed of the myosin heavy chain Myo2p and essential and regulatory light chains Cdc4p and Rlc1p) (Fankhauser *et al.*, 1995; Carnahan and Gould, 2003; Roberts-Galbraith *et al.*, 2009; Laporte *et al.*, 2011; Willet *et al.*, 2015, 2018; McDonald *et al.*, 2017). The second explanation is that Cdc15p supports the anchoring of the contractile ring by promoting the transport of Bgs1p from the Golgi to the division plane where Bgs1p produces the septum material and stabilizes the position of the contractile ring (Cortes *et al.*, 2002; Arasada and Pollard, 2014). The role of Imp2p in supporting the connection of the contractile ring to the plasma membrane and cell wall remains unknown.

This article was published online ahead of print in MBoC in Press (http://www.molbiolcell.org/cgi/doi/10.1091/mbc.E22-06-0221) on October 26, 2022.

†Equal contributions.

Author contributions: C.L.: conceptualization, methodology, writing and editing, project administration, and funding. K.B.-J. and B.L.: data acquisition, analysis, and validation and writing and editing. B.C.: data acquisition and analysis and writing and editing. Z.L.T.: data analysis and validation and editing.

*Address correspondence to: Caroline Laplante (claplan@ncsu.edu).

Abbreviations used: CDF, cumulative distribution function; F-BAR, Fer/CIP4 homology Bin-Amphiphysin-Rvs; IDR, intrinsically disordered region; IQGAP, isoleucine-glutamine GTPase-activating protein; LatA, latrunculin A; mEGFP, monomeric enhanced green fluorescent protein; RDD, radial density distribution; SCPR, search capture pull release; SH3, Src Homology 3; SMLM, single molecule localization microscopy; TMR, tetramethylrhodamine.

The structural similarities between Imp2p and Cdc15p and phenotypic similarities between cells expressing mutations in *imp2* and *cdc15* have concealed their distinctive roles during cytokinesis. Cdc15p and Imp2p share similar structural features with an N-terminal plasma membrane binding F-BAR domain followed by an intrinsically disordered region (IDR) and a C-terminal protein–protein interaction Src Homology 3 (SH3) domain. Imp2p and Cdc15p have partially interchangeable F-BAR, IDR, and SH3 domains (Roberts-Galbraith *et al.*, 2010; McDonald *et al.*, 2016; Lee *et al.*, 2018; Mangione *et al.*, 2019; Bhattacharjee *et al.*, 2020; Magliozzi *et al.*, 2020; Willet *et al.*, 2021). Imp2p and Cdc15p even share SH3 domain binding partners including Fic1p and Sbg1p. Some differences between the two proteins include the distinct impact of their regulation by phosphorylation. While prolonged phosphorylation of the IDR of Cdc15p leads to aberrations in membrane binding, the phosphorylation of the IDR of Imp2p is constitutive and necessary for proper contractile ring anchoring (Willet *et al.*, 2021). Finally, Cdc15p is involved in both cytokinesis and endocytosis, whereas Imp2p localizes only to the contractile ring, suggesting that its function is restricted to cytokinesis (Demeter and Sazer, 1998; Arasada and Pollard, 2011).

Cdc15p is a component of cytokinesis nodes, large protein complexes distributed in a broad band around the cell center that coalesce to form the contractile ring (Wu *et al.*, 2003, 2006; Moseley *et al.*, 2009). Quantitative single molecule localization microscopy (SMLM) in live cells revealed the molecular organization of node proteins (Laplante *et al.*, 2016b; Bellingham-Johnstun *et al.*, 2021). Node proteins closest to the plasma membrane form the core of the node and include Cdc15p, the IQGAP homologue Rng2p, and the tips of the Myo2 tails, whereas the motor heads of the Myo2 molecules fan into the cytoplasm, poised to bind a somewhat random network of actin filaments ~60 nm away from the plasma membrane. The molecular organization of the node thus hints that these protein complexes may act as anchors that link the main bundle of actin filaments to the plasma membrane and the cell wall. We previously investigated the role of Cdc15p on the mechanical properties of the contractile ring. We used laser ablation to sever the contractile ring of cells depleted of Cdc15p and found that Cdc15p impacts the stiffness of the contractile ring, suggesting that nodes bear the tension load of the contractile ring (Moshtohry *et al.*, 2022).

Here, we investigate the molecular organization of Imp2p in the contractile ring and its impact on the mechanical properties of the contractile ring. Analysis of the recoil displacement of severed contractile ring tips after laser ablation in Δ*imp2* cells, cells with a deletion of the *imp2* gene, shows that Imp2p contributes to the stiffness of the contractile ring similar to Cdc15p. SMLM in live cells revealed that Imp2p clusters within the contractile ring similar to Cdc15p nodes. However, the Imp2p clusters are smaller than the Cdc15p nodes and each cluster contains approximately eight dimers of Imp2p, whereas each node contains approximately 12 dimers of Cdc15p. We measured that the contractile ring contains fewer Imp2p clusters than Cdc15p nodes. Yet Imp2p and Cdc15p reciprocally affect the levels of each other in the contractile ring, indicating that they influence each other. Unlike Cdc15p nodes, Imp2p clusters depend on the actin network for their stable interaction with the plasma membrane at the division plane, underlining an important difference between the two complexes.

RESULTS

Imp2p impacts the stiffness of the constricting contractile ring

Cells that lack *imp2* have been shown to exhibit multiple cytokinesis defects, including defective ring disassembly and defective septation leading to multiseptated cells (Figure 1A) (Demeter and Sazer, 1998; Martin-Garcia and Valdivieso, 2006). On a population level, Δ*imp2* cells expressing mEGFP-Myo2p and stained with Fluorescent Brightener 28 (FB28) showed a degree of ring offset similar to that of cells depleted of Cdc15p using the *Pnmt81* promoter (see *Materials and Methods* for details) (Arasada and Pollard, 2014; McDonald *et al.*, 2015). This result suggests that rings either slid off the center of the cell after assembly or assembled off center in Δ*imp2* cells (Figure 1B). To determine whether rings assembled at the cell center and slid away, we measured ring sliding in time-lapse micrographs of wild-type and Δ*imp2* cells expressing mEGFP-Myo2p (Figure 1C). In Δ*imp2* cells, rings assembled at the cell center and slid away from that initial position over time comparable to the ring sliding phenotype observed in Cdc15p-depleted cells (Figure 1, C and D) (Arasada and Pollard, 2014; McDonald *et al.*, 2015).

Laser ablation of the contractile ring can reveal otherwise undetectable features about its structure, including mechanical properties (Silva *et al.*, 2016; Moshtohry *et al.*, 2022). We recently described the contribution of Cdc15p to the stiffness of the constricting contractile ring using laser ablation (Moshtohry *et al.*, 2022). We hypothesized that Imp2p may impact the mechanical properties of the ring in a manner distinct from that of Cdc15p that would reveal its specific functions in cytokinesis. We used laser ablation to sever constricting contractile rings in wild-type and Δ*imp2* cells expressing mEGFP-Myp2p to highlight the bundle of actin filaments in the ring (Figure 1E, Supplemental Figure 1A, and *Materials and Methods*) (Moshtohry *et al.*, 2022). We focused on contractile rings that were 20–50% constricted to avoid confounding results with nonconstricting contractile rings, maturing rings before the onset of constriction, that may have distinct mechanical properties. We imaged each cell before laser ablation, severed the contractile ring, and imaged the response every second for up to ~5 min.

After severing the constricting contractile ring in wild-type cells, the severed tips recoiled away from one another, revealing a growing gap in the ring (Figure 1E) (Moshtohry *et al.*, 2022). We interpreted this response as the local release of tension present in the constricting contractile ring before ablation (McDargh *et al.*, 2021). Consistent with this interpretation, the rate of ring constriction slowed down, but constriction did not stop after laser ablation, suggesting that severing the ring causes the local release of tension while tension is at least partially maintained in the remaining ring fragment away from the cut site (Moshtohry *et al.*, 2022). Eventually, the severed tips stopped recoiling. We observed the same response in Δ*imp2* cells except that the severed tips recoiled farther from one another, revealing a larger gap in the ring (Figure 1E).

To determine the impact of Imp2p on the mechanical properties of the contractile ring, we tracked the position of the severed tips during the recoil phase and calculated the recoil displacement as the distance of the severed tips from their initial position immediately after the cut over time. The recoil displacements of the severed tips in both wild-type and Δ*imp2* cells followed an exponential profile as expected for a material with viscoelastic properties (Figure 1F) (Kumar *et al.*, 2006; Colombelli *et al.*, 2009; Silva *et al.*, 2016; Roca-Cusachs *et al.*, 2017; Moshtohry *et al.*, 2022). The mean recoil displacement of the severed tips ΔL fits to a single exponential, $\Delta L(t) = A\left(1 - e^{-\frac{t}{\tau}}\right)$. For severed rings in wild-type cells, we measured a total magnitude of the recoil after ablation, A = 0.41 ± 0.01 μm (mean ± SE on the least squares fit, n = 18 severed tips), and a timescale of viscoelastic recoil, τ = 22 ± 1 s (mean ± SE). For Δ*imp2* cells, both the recoil magnitude of the severed tips and timescale

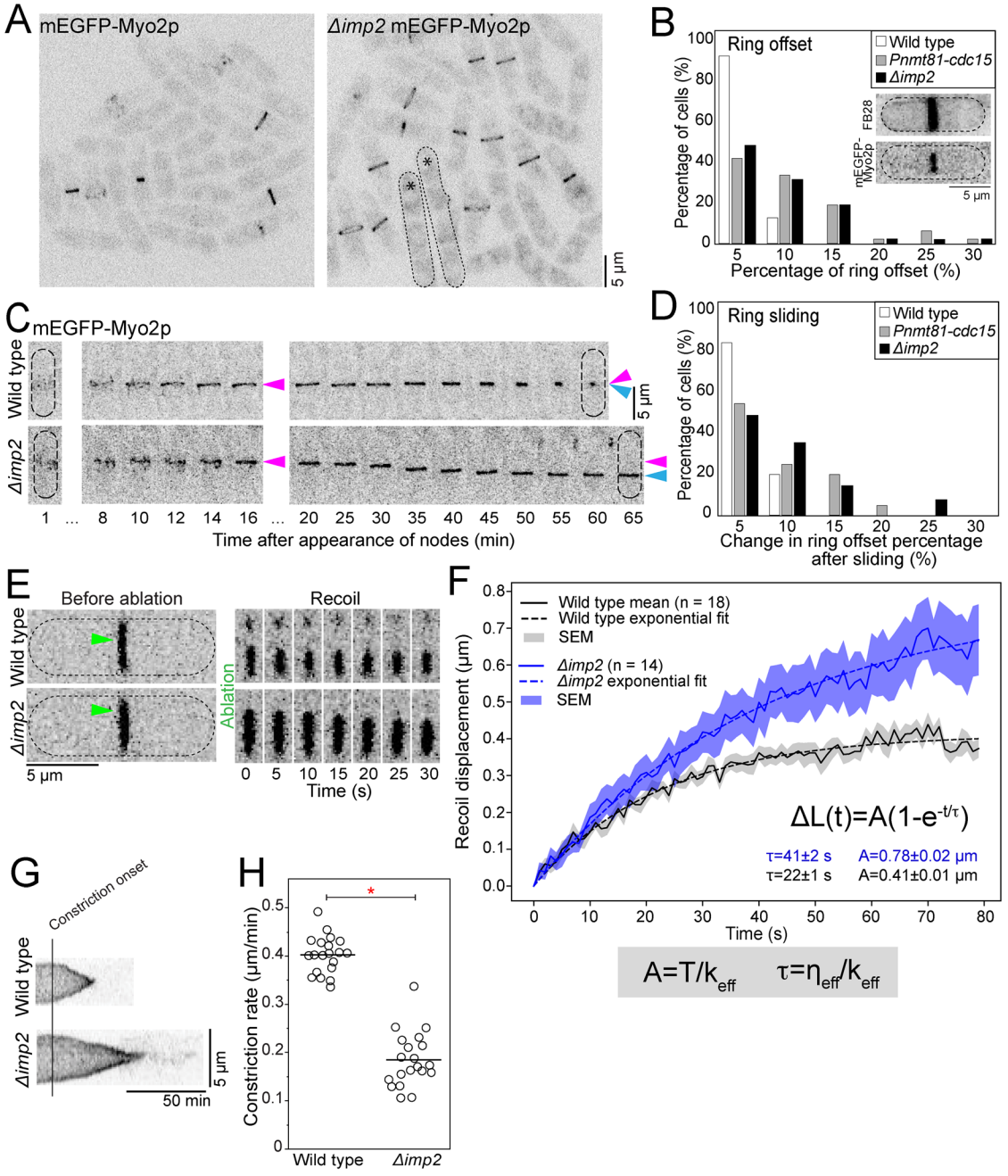

FIGURE 1: Imp2p impacts the stiffness of the constricting contractile ring. (A) Confocal fluorescence micrographs of fields of wild-type (left) and Δ*imp2* (right) cells. Asterisks, multiseptated cells. Dotted line, cell outline. (B) Graph of the ring offset measured in still images. $n = 50$ cells for each genotype. Inset, confocal micrographs of a representative wild-type mEGFP-Myo2p cell stained with FB28 that has a ring with a 2% offset. Dotted line, cell outline. (C) Time-lapse montages of wild-type and Δ*imp2* cells showing the position of the ring over time. Magenta arrowheads, position of ring at the time of assembly. Blue arrowheads, position of the ring at the end of cytokinesis (wild type) or maximum displacement (Δ*imp2*). (D) Graph of the change in the percentage of ring offset measured after ring sliding in time-lapse movies. $n = 21$ cells for each genotype. (E) Time-lapse montages of wild-type (top) and Δ*imp2* (bottom) cells before and after laser ablation. Green arrowheads, sites of ablation. (F) Graph of the recoil displacement of severed tips in wild-type and Δ*imp2* cells. Gray shaded box, equations representing our framework. (G) Kymographs of constricting contractile ring aligned at constriction onset in a representative wild-type (top) and Δ*imp2* (bottom) cell. (H) Swarm plot showing the constriction rate of the contractile rings in wild-type and Δ*imp2* cells. Line, average constriction rate. $n = 20$ cells for each genotype. Asterisk, $p < 0.05$ by Student's *t* test. All micrographs are shown as inverted grayscale LUT.

nearly doubled compared with wild type (A = 0.78 ± 0.02 μm, mean ± SE, n = 14) (τ = 41 ± 2 s, mean ± SE). The experimental displacement curve for Δ*imp2* cells did not reach a plateau under our experimental conditions, likely because the severed tips recoiled out of the imaging plane, indicating that our reported values of A and τ may represent lower limits on these values in Δ*imp2* cells (Supplemental Figure 1A). The values of A and τ in Δ*imp2* cells are reminiscent of those measured in Cdc15p-depleted cells

(A = 0.75 ± 0.01 μm and τ = 30 ± 1 s) (Supplemental Figure 1B) (Moshtohry *et al.*, 2022).

We calculated the impact of Imp2p on the effective stiffness k_{eff} and effective viscous drag η_{eff} of the contractile ring based on our framework for the contractile ring as a viscoelastic material under tension T_0 (McDargh *et al.*, 2021; Moshtohry *et al.*, 2022). Both A and τ describe the displacement profile of the severed tips and are influenced by the mechanical properties of the contractile ring as $A = T_0/k_{eff}$ and $\tau = \eta_{eff}/k_{eff}$ (Figure 1F). Given the relationship between A and k_{eff} and the increased A, our data suggest that k_{eff} of the contractile ring decreases in Δ*imp2* cells. In addition, deleting Imp2p likely impacts k_{eff} more than η_{eff} as A and τ increased by similar factors and both A and τ rely on k_{eff}. We measured a reduction in the constriction rate in Δ*imp2* cells of ~50% compared with wild type, suggesting that the total tension in the contractile ring is decreased in Δ*imp2* cells (Figure 1, G and H). This result is consistent with the reduction in constriction rate measured in a phosphomutant allele of *imp2* (*imp2-17E*) (Willet *et al.*, 2021). With the likelihood that T_0 is decreased in the contractile rings of Δ*imp2* cells, the viscous drag may also be decreased compared with wild type. Nevertheless, deleting *imp2* impacts the stiffness more than the viscous drag.

Wild-type severed rings heal by creep while those of Δ*imp2* heal by strand capture

Following ablation, most severed contractile rings in both wild-type and Δ*imp2* cells were competent to heal the gap caused by the recoil (Figure 2, A and B). In wild-type cells, the severed tips stopped recoiling after 43 ± 21 s (n = 18 severed tips) and in most cells the gap in the severed contractile ring healed over the following 82 ± 33 s (n = 9 severed tips). Because many severed tips in Δ*imp2* cells recoiled out of the imaging plane, we could determine neither when recoil ended nor the duration of healing (Figure 2A and Supplemental Figure 1A). In wild-type cells, the gap closed by 172 ± 67 min (n = 9) after ablation, as determined by mEGFP-Myp2p signal joining together across the gap. In Δ*imp2* cells, the healing took slightly longer and mEGFP-Myp2p signal filled the gap by 199 ± 56 min (n = 8) after ablation.

The healing process appeared differently between wild-type and Δ*imp2* cells. Tracking the motions of the severed tips of wild-type rings during the healing phase showed their progressive creeping motion toward one another until the tips connected (Figure 2C and Supplemental Figure 2A). The severed tip underwent rapid back-and-forth motions during this creeping (Supplemental Figure 2A). All observed severed wild-type rings that healed (11 rings) healed by this creeping motion. In most severed rings of Δ*imp2* cells (five out of eight severed Δ*imp2* rings that healed), however, a faint mEGFP-Myp2p signal suddenly appeared across the entire gap and the signal then gradually intensified over time (Supplemental Figure 2A). Tracking of the severed tips in those Δ*imp2* rings showed some initial creeping motion of the tips as observed in wild type. But tracking ended when the mEGFP-Myp2p signal suddenly appeared and filled the gap (Figure 2C and Supplemental Figure 2A). We observed this mechanism of healing in severed rings of Δ*imp2* cells with large and small gaps (Figure 2A and Supplemental Figure 2A). Contractile rings of Δ*imp2* cells that failed to heal during our 5 min acquisition after ablation did not show this behavior. Instead, their severed tips remained at the same position after the completion of the recoil phase (Supplemental Figure 2B). The sudden appearance of mEGFP-Myp2p signal across the gap in the severed rings suggests that a preassembled strand or bundle of actin filaments labeled with mEGFP-Myp2p joined the discontinuous ring. The strands did not laterally sweep into the gap from within the imaging

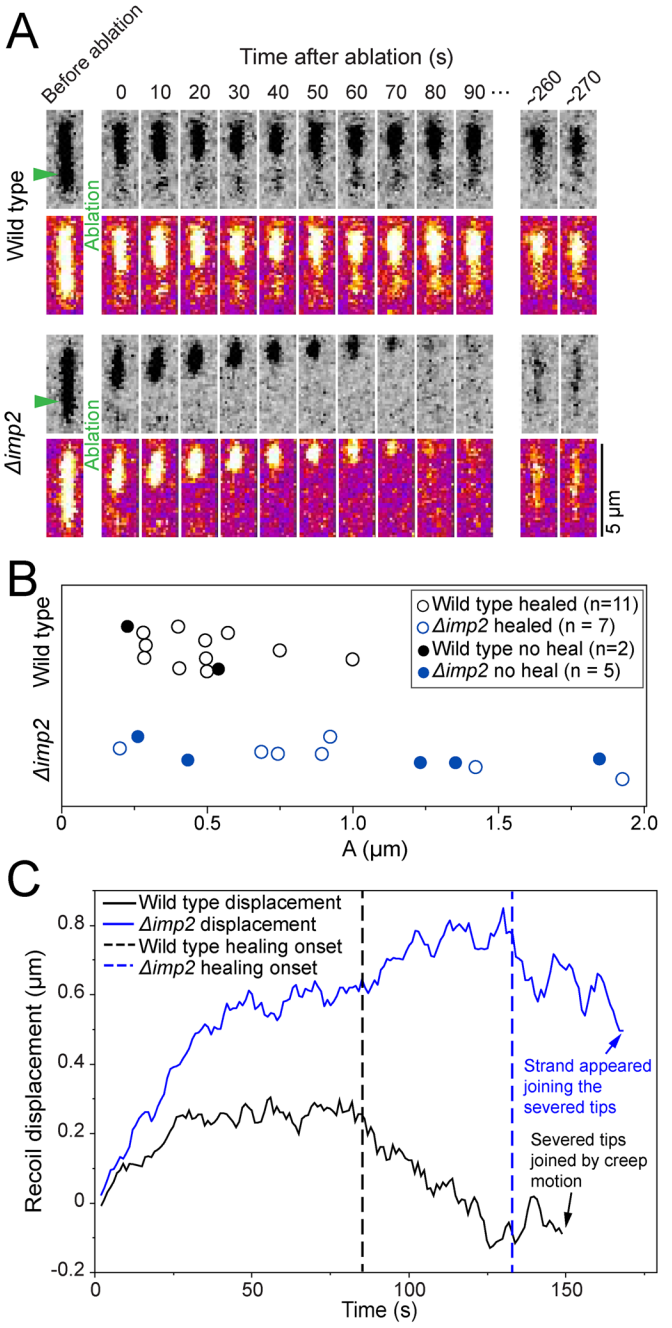

FIGURE 2: Severed contractile rings of Δ*imp2* cells can heal. (A) Recoil and healing of typical severed wild-type (top) and Δ*imp2* (bottom) cells where the visible severed tip recoils out of the imaging plane. Top row, inverted gray LUT. Bottom row, Fire LUT. Green arrowheads, sites of ablation. (B) Graph showing the ability of a severed wild-type or Δ*imp2* contractile ring to heal after ablation vs. maximum displacement A. (C) Graph of the recoil displacement (5 s rolling average) for a single severed tip of a wild-type or Δ*imp2* contractile ring showing recoil and healing. Dotted lines, time at which healing begins. Tracking of the severed tips of a wild-type ring show the progressive creeping motion until the tips joined across the gap. Tracking of the severed tips of the Δ*imp2* ring shows initial progressive creeping motion of the tip until tracking appearance of a strand ~170 s after ablation.

plane, suggesting that they emerged from deeper into the cell, below the imaging plane. Although our current experimental setup limits acquisition to a single imaging plane, preventing us from

observing material across the thickness of the ring, dynamic bundles of actin filaments labeled with mEGFP-Myp2p cross the middle of the contractile ring during constriction and may be the source of the strands we observed during the healing of severed Δ*imp2* rings (Laplante *et al.*, 2015).

Reciprocal influence between Imp2p and Cdc15p in the contractile ring

To understand how Imp2p influences the mechanical properties of the contractile ring, we measured the local number of cytokinesis proteins in the contractile ring of Δ*imp2* cells and wild-type cells. We measured the number of polypeptides of type II myosins, mEGFP-Myo2p and mEGFP-Myp2p, and of actin (labeled with *Pcof1-mEGFP-LifeAct*) in wild-type and Δ*imp2* cells (Wu and Pollard, 2005; Wu *et al.*, 2008; Malla *et al.*, 2022). In brief, we acquired single time point z-stacks through the entire cell volume. We projected the images, corrected them for camera noise and uneven illumination, and measured the local fluorescence intensity within the contractile ring for each mEGFP-tagged protein of interest. Finally, we use the local fluorescence intensity values to calculate the total number of polypeptides per contractile ring using a standard curve. We found no significant difference in the amounts of either type II myosins or actin in the contractile ring of Δ*imp2* cells compared with wild-type cells, suggesting that Imp2p does not impact the tension or the mechanical properties of the contractile ring by altering the total amount of these proteins within the contractile ring (Figure 3A).

We determined the levels of mEGFP-Cdc15p in Δ*imp2* and wild-type cells as described above. We measured an ~25% decrease in the mean number of polypeptides of Cdc15p in Δ*imp2* cells compared with wild type across all ring diameters (Figure 3A). This difference was significant in larger rings (>2 µm in diameter, $p = 0.0059$) and in rings of smaller diameter (<2 µm, $p = 0.0420$, as measured by Student's *t* test). To determine whether Cdc15p also affects the levels of Imp2p, we measured the local amount of Imp2p-mEGFP in the contractile rings of cells depleted of Cdc15p. We found that depleting Cdc15p caused an ~50% decrease in the amount of Imp2p-mEGFP in contractile rings compared with wild type (Figure 3A). Therefore, our results suggest that Δ*imp2* cells contain ~75% of the total amount of Cdc15p, whereas contractile rings in Cdc15p-depleted cells contain ~50% of the total amount of Imp2p.

Depleting Cdc15p results in a delayed accumulation of Bgs1p to the contractile ring and a decreased total amount of Bgs1p throughout constriction (Arasada and Pollard, 2014). Contractile ring sliding had been attributed to the decreased amount of Bgs1p in cells depleted of Cdc15p. As deleting *imp2* results in an ~25% decrease of Cdc15p and mutations or deletion of *imp2* result in ring sliding, we sought to determine whether Imp2p impacts the amount of Bgs1p in the contractile ring by measuring the total amounts of GFP-Bgs1p in contractile rings of Δ*imp2* and wild-type cells (Willet *et al.*, 2021). We found no significant difference in the total amounts of GFP-Bgs1p in the rings of Δ*imp2* cells compared with wild type, suggesting that although the lack of Imp2p causes only a 25% decrease in Cdc15p, that decrease is insufficient to cause a noticeable decrease in GFP-Bgs1p (Figure 3A). Our measurements suggest that contractile ring sliding in Δ*imp2* cells is not caused by a reduction in Bgs1p. Instead, the ring sliding phenotype may be caused by the combination of the lack of Imp2p and reduction of Cdc15p resulting in weakened connections between the ring and the plasma membrane.

Complexes containing approximately eight dimers of Imp2p assemble in the contractile ring

Our observation that Imp2p and Cdc15p reciprocally impact their levels in the ring suggests that they may assemble into a larger complex. Consistent with this hypothesis, SMLM of contractile rings in fixed cells showed that the N- and C-termini of Cdc15p and Imp2p localize in the same functional layers of the contractile ring (McDonald *et al.*, 2017). We used SMLM in live cells to determine the molecular organization of Imp2p in the constricting contractile ring. We tagged Imp2p at either the N- or the C-terminus with mEos3.2 and acquired SMLM data at 200 fps for 40 s (8000 camera frames; see *Materials and Methods*) (Laplante *et al.*, 2016a,b; Bellingham-Johnstun *et al.*, 2021). For comparison, we acquired both the N- and C-terminal mEos3.2 tagged Cdc15p. To enrich for cells in cytokinesis, we used *cdc25-22* mutation to arrest the cells at the G2-M phase of the cell cycle and released them into mitosis before imaging. Cells expressing either the N- or C-terminal tagged Cdc15p showed the typical pattern of clustered emitters within the contractile ring (Laplante *et al.*, 2016b). Similarly, cells expressing either of the N- or C-terminal mEos3.2 tagged Imp2p constructs showed clusters of emitters aligned into rings at the division plane, suggesting that Imp2p assembles into protein complexes within the constricting contractile ring (Figure 3, B and C).

To characterize individual Imp2p protein clusters while avoiding neighboring clusters within the dense contractile ring, we reconstructed the data using 1000 camera frames (5 s), cropped the protein complexes and analyzed them to measure their radial density distribution (RDD) and dimensions (Figure 3D) (Laplante *et al.*, 2016b; Bellingham-Johnstun *et al.*, 2021). As controls, we measured the radii of mEos3.2-Cdc15p and Cdc15p-mEos3.2 nodes and obtained 37 and 45 nm, respectively, comparable to our previous measurements (Laplante *et al.*, 2016b; Bellingham-Johnstun *et al.*, 2021). These measurements are consistent with the distribution of the N-terminal F-BAR domains grouping into smaller-size clusters than the C-termini, located at the end of both the IDR and SH3 domains (Laplante *et al.*, 2016b). We measured the radii of the N- and C-termini of Imp2p. Similarly, we found that the N-termini of Imp2p were smaller than their C-termini. Our measurements show a radius of 31 nm for mEos3.2-Imp2p and 37 nm for Imp2p-mEos3.2 (Figure 3, D and E). Both N- and C-termini of Imp2p are smaller than those of Cdc15p (Figure 3, D and E, and Supplemental Figure 3, A and B).

We counted the localized emitters per cluster using the 5 s reconstructed data. We measured 58 ± 20 and 65 ± 19 localized emitters per the mEos3.2-Cdc15p and Cdc15p-mEos3.2 node, respectively, comparable to our previous measurements (Bellingham-Johnstun *et al.*, 2021). In contrast, we measured 42 ± 15 and 43 ± 17 localized emitters per the mEos3.2-Imp2p and Imp2p-mEos3.2 cluster, respectively (Figure 3F). Our measurements suggest an ~2/3 ratio of number of localized emitters of Imp2p to Cdc15p. Although the number of localized emitters per protein complex does not directly translate into numbers of proteins due to the stochastic blinking behavior of mEos3.2, the number of emitters scales with the number of proteins per complex (Laplante *et al.*, 2016b). In previous work, we estimated 10–12 dimers of Cdc15p per node, suggesting that there are approximately six to eight dimers of Imp2p per cluster (Laplante *et al.*, 2016b).

We calculated the total amount of Imp2p-mEGFP protein in the contractile ring by quantitative confocal microscopy as described above. In rings that were 20–50% constricted, we calculated that the total amount of Imp2p-mEGFP is ~1/2 of that of mEGFP-Cdc15p (Figure 3G). An ~2/3 ratio of localized emitters for Imp2p to Cdc15p per node combined with an ~1/2 ratio of total Imp2p to Cdc15p per

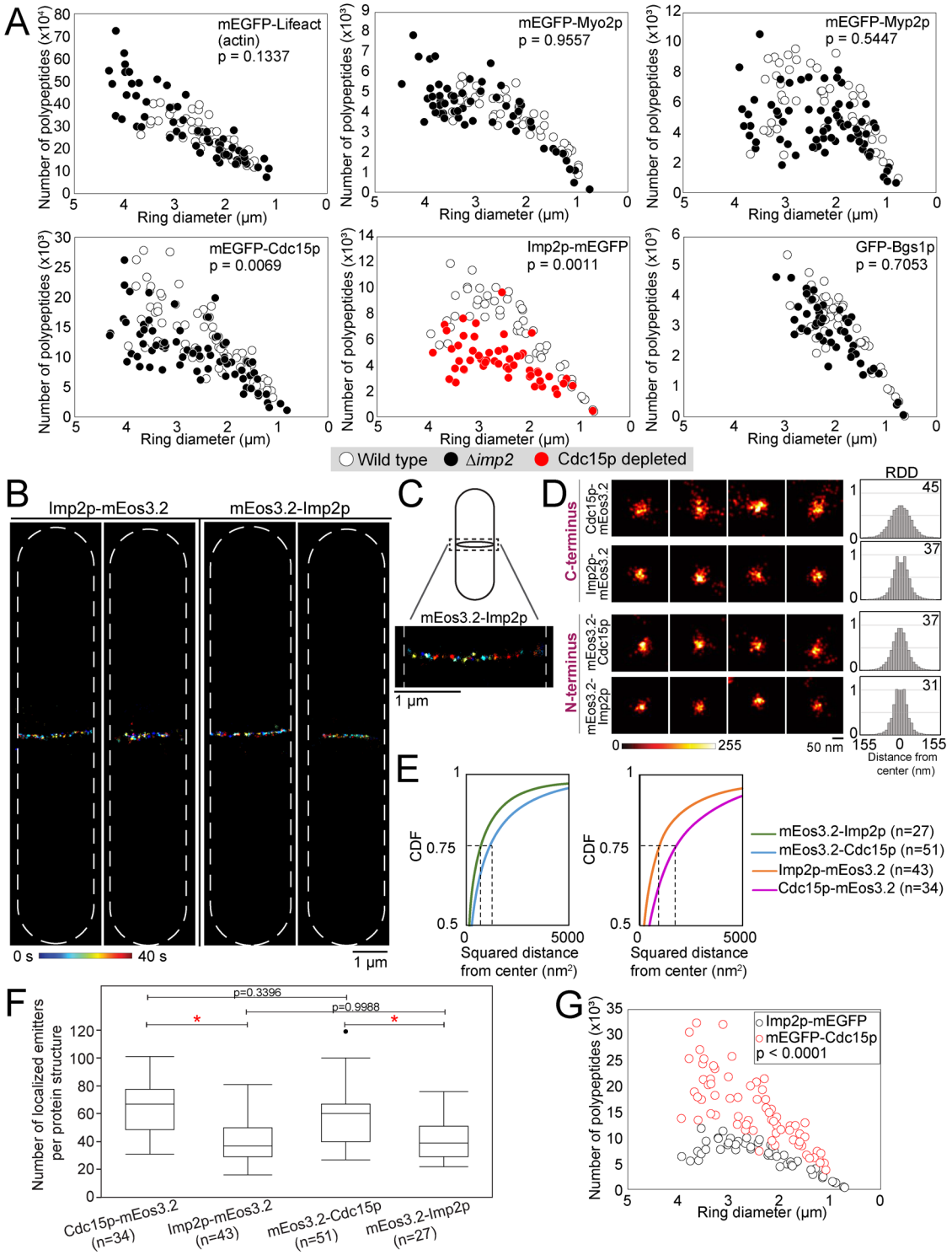

FIGURE 3: Imp2p can cluster in the contractile ring. (A) Plots of the distribution of the number of polypeptides per ring for cytokinesis proteins in wild-type, Δ*imp2*, and Cdc15p-depleted cells. Resulting actin monomer values from strains containing the mEGFP-Lifeact construct were scaled to reflect that the Lifeact construct labels 6% of polymerized actin (Malla *et al.*, 2022). Differences between the distributions of polypeptides were determined by a standard least squares model; *p* values stated on each plot. (B) Examples of SMLM of Imp2p-mEos3.2 (left) and mEos3.2-Imp2p (right) in cells with contractile rings at different stage of constriction. (C) Representative image of a cropped contractile ring in a cell expressing mEos3.2-Imp2p. (D) Four representative cropped protein clusters from contractile rings of cells expressing either N- or C-terminal tagged Imp2p or Cdc15p (left). Protein clusters are color coded for density. Graphs of RDD (right) and radii in nanometers (top right of each graph). (E) Overlaid CDF plots of mEos3.2-Imp2p and mEos3.2-Cdc15p (left) and Imp2p-mEos3.2 and Cdc15p-mEos3.2 (right) in protein clusters of the contractile ring. Dotted line, squared distance away from center that contains 75% of localized emitters. Full CDF plots in Supplemental Figure 3B. Number

ring suggest that there are fewer Imp2p complexes than Cdc15p nodes per ring.

Imp2p requires actin for stable localization to the plasma membrane

The similarities in protein structure, localization within the contractile ring, and impact on the mechanical properties in the contractile ring suggest that Cdc15p and Imp2p may be found in the same structure. Upon treating cells with a low concentration of latrunculin A (LatA), nodes that were corralled in the contractile ring dispersed away from the division plane yet remained attached to the plasma membrane (Bellingham-Johnstun *et al.*, 2021). To determine whether Cdc15p and Imp2p colocalize, we treated cells coexpressing Cdc15p-HALO*TMR and Imp2p-mEGFP with a low concentration of LatA (see *Materials and Methods*). We hypothesized that Imp2p clusters and Cdc15p nodes may disperse from the contractile ring either together or separately, depending on their interactions. Within 10 min of LatA addition, Cdc15p-HALO*TMR nodes began to disperse away from the plane of cell division, as previously observed for nodes labeled with mEGFP-Myo2p (Figure 4A) (Bellingham-Johnstun *et al.*, 2021). However, Imp2p-mEGFP did not exit the contractile ring as membrane-bound clusters. Instead, the Imp2p-mEGFP signal gradually disappeared from the contractile ring over a period of ~50 min (Figure 4, A and B). These observations suggested that Imp2p diffused back into the cytoplasm as the actin of the contractile ring depolymerized. After ~40 min of LatA treatment, we began to observe transient speckles of Imp2-mEGFP signal appearing at the plasma membrane throughout the cell surface and sometimes appearing adjacent to the nucleus (Figure 4, A and B). These Imp2p-mEGFP accumulations were visible for only approximately one to three consecutive time points (1–3 min) before disappearing. These observations suggest that the localization of Imp2p to the contractile ring and its interaction with the plasma membrane depend on the presence of actin. Although this experiment did not determine whether Imp2p and Cdc15p localize within the same larger protein complex, our results suggest that if they do coexist in such combined complexes the interactions necessary to form these complexes would depend on the presence of actin filaments.

DISCUSSION

The molecular organization of the contractile ring influences its mechanical properties and governs its function, but these relationships remain unknown. We used SMLM in live fission yeast cells and laser ablation to reveal the organization of the putative anchor protein Imp2p and determine its impact on the mechanical properties of the contractile ring. Our laser ablation results suggest that Imp2p, like Cdc15p, primarily impacts the stiffness of the constricting contractile ring (Moshtohry *et al.*, 2022). Although they may also impact the viscous drag, that effect is minimal compared with the impact on the stiffness. Such minimal impact on the viscous drag may be due to the large number of molecular interactions that contribute to the effective viscous drag, including molecular interactions between actin filaments and between the bundle of actin and the membrane. To explain the impact of Imp2p and Cdc15p on the effective stiffness of the contractile ring, we assume that they are subunits of complexes that function as Hookean springs. Upon severing the ring by laser ablation, the tension is released locally, and the springs stretch to a maximum distance *A*. The stiffness of the springs determines that maximum distance. When subjected to the same amount of tension force, a stiffer spring stretches to a shorter maximum distance, whereas a softer spring stretches to a larger maximum distance. Our results suggest that deleting *imp2* or depleting Cdc15p results in a softer spring that can stretch to a larger maximum distance. Assuming that Imp2p and Cdc15p are critical factors in the overall anchoring mechanism, a softer anchoring mechanism is presumably less effective at bearing the load of the constricting contractile ring. This could lead to inefficient transmission of contractile force from the actin bundle to the plasma membrane and cell wall, resulting in a slower rate of constriction.

Understanding how Imp2p anchors the contractile ring and how it may impact the mechanical properties of the ring requires knowledge about its molecular organization. Using SMLM and confocal imaging in live fission yeast cells, we found that Imp2p can assemble into complexes within the contractile ring and that actin is required for the stable association of Imp2p with the plasma membrane. Our quantitative measurements also revealed a reciprocal relationship between the levels of Imp2p and Cdc15p. Although we do not yet know the molecular basis of this reciprocal influence, one possible explanation is that Cdc15p nodes and Imp2p complexes physically interact. Imp2p complexes and Cdc15p nodes may be subunits of transient or stable larger complexes within the constricting contractile ring. The formation of such large protein complexes containing both Imp2p and Cdc15p and the rest of the node proteins would provide a mechanism for Imp2p to link the actin network to the plasma membrane and act as an anchor. Indeed, by working with Cdc15p node proteins, Imp2p would indirectly link the actin network to the plasma membrane. The physical interaction of Imp2p with the nodes could allow Imp2p to sense the actin network through the node proteins, promoting its stability at the membrane. The removal of the actin network by LatA treatment may in turn change the conformation of the proteins within the large complexes, causing the detachment of Imp2p. The formation of these large complexes could also explain the ability of Imp2p and Cdc15p to reciprocally influence the levels of one another. For example, the presence of Imp2p may improve the stability of Cdc15p in the contractile ring and vice versa. Possible candidates for bridging Imp2p and Cdc15p include their known shared binding partners Fic1p and Sbg1p. Indeed, Fic1p and Sbg1p can interact with all three cytokinesis F-BAR domain containing proteins, Cdc15p, Imp2p, and Rga7p, possibly relating these different components of the general anchoring mechanism (Roberts-Galbraith *et al.*, 2009; Bohnert and Gould, 2012; Martin-Garcia *et al.*, 2014; Ren *et al.*, 2015; Sethi *et al.*, 2016; Bhattacharjee *et al.*, 2020). Future work will determine whether Imp2p and Cdc15p can coassemble into larger protein complexes and the molecular interactions that promote their assembly. Alternatively, Imp2p and Cdc15p may not physically interact and instead Imp2p could be part of a distinct anchoring protein

of nodes analyzed per marker listed in parentheses. (F) Number of localized emitters per protein complex for N- or C-terminal tagged Imp2p or Cdc15p. Number of nodes analyzed per marker listed in parentheses. Asterisk, $p < 0.05$ by Tukey's HSD. (G) Plots of the distribution of the number of polypeptides per ring for Imp2p-mEGFP and mEGFP-Cdc15p in wild-type cells. Differences between the distributions of polypeptides was determined by a standard least squares model.

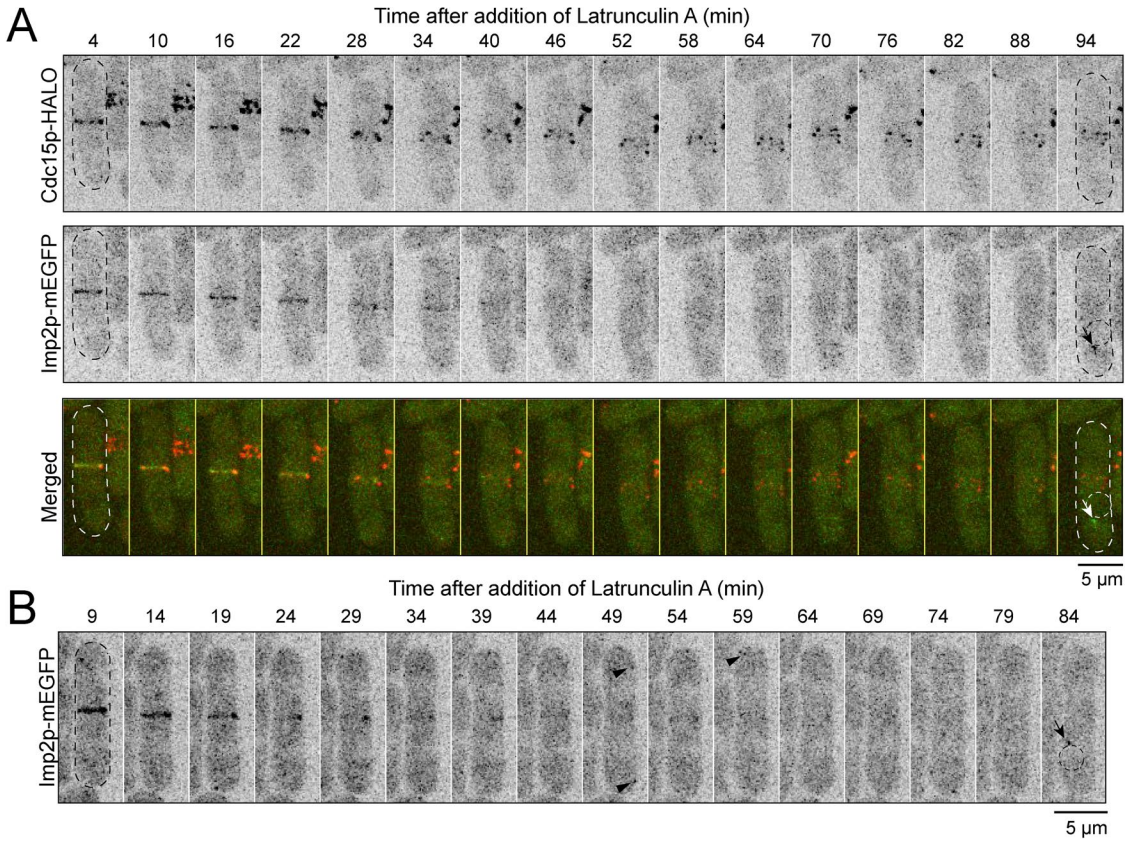

FIGURE 4: Imp2p localization at the plasma membrane depends on actin. (A) Time-lapse montages of cells coexpressing Cdc15p-HALO*TMR and Imp2p-mEGFP after the addition of 5 µM LatA. Arrow, perinuclear cluster of Imp2p. Dotted circular outline, nucleus. (B) Time-lapse montages of strains expressing Imp2p-mEGFP after the addition of 10 µM LatA. Arrow, perinuclear cluster of Imp2p. Arrowheads, speckles of Imp2p. Dotted circular outline, nucleus.

complex that links the actin network to the plasma membrane. In such case, the roles of Cdc15p nodes and Imp2p complexes may be complementary. If so, it will be critical to identify the other members of the Imp2p protein complex to understand how Imp2p interacts with actin to anchor the contractile ring and how the presence of the actin influences the stability of Imp2p at the membrane.

Severed rings in wild-type cells heal, suggesting the presence of a mechanism that mends discontinuities within the contractile ring. Approximately 60% of the severed rings in Δ*imp2* cells healed, while severed rings in cells depleted of Cdc15p rarely healed. Although we did not measure a strong correlation between the amplitude of recoil *A* and the ability of a ring to heal in Δ*imp2* cells, this relationship was measured for ablated rings in cells depleted of Cdc15p (Moshtohry *et al*., 2022). We observed distinct methods of healing between wild-type and Δ*imp2* cells. In wild-type cells and the few Cdc15p-depleted cells that showed ring healing, the severed tips gradually extend across the gap, presumably by the polymerization of new actin filaments that progressively become stabilized at the plasma membrane by anchors present in the gap. This method, termed "creep," closes the gap slowly and may be most efficient at closing smaller gaps of <1 µm. In contrast, Δ*imp2* cells exhibited the sudden appearance of a strand labeled with mEGFP-Myp2p across the gap. Our interpretation of this healing method, termed "strand capture," is that a prefabricated strand of actin filaments attaches to the plasma membrane possibly by anchors present in the gap. This method may thus be more suitable to heal larger gaps as a long strand can instantly bridge the gap between the two severed tips. It is likely that the two mechanisms combine to heal gaps in wild-type cells to ensure the robustness of cytokinesis, yet one mechanism may dominate in certain mutant backgrounds. Although the molecular mechanisms underlying these two healing pathways remain unknown, the search-capture-pull-release (SCPR) mechanism is a strong candidate for the creep healing pathway (Vavylonis *et al*., 2008; Moshtohry *et al*., 2022). Using the SCPR mechanism, molecules of formin Cdc12p present in Cdc15p nodes polymerize new actin filaments that become bound by the Myo2 molecules in neighboring nodes. It is likely that nodes are also responsible for the capturing of strands in the strand capture healing pathway. Severed constricting contractile rings in *Caenorhabditis elegans* are also competent to heal, indicating that the core mechanisms that heal discontinuous contractile rings may be conserved across species (Silva *et al*., 2016). Based on our results, the anchoring mechanism influences the ability of a ring to heal a gap and the method utilized to heal this gap. Therefore, understanding the different aspects of the healing mechanisms may reveal unknown functions of the anchoring complexes.

MATERIALS AND METHODS

Request a protocol through *Bio-protocol*.

Strains, growing conditions, and genetic and cellular methods

Supplemental Table S1 lists the *Schizosaccharomyces pombe* strains used in this study. The strains were created using PCR-based gene targeting to integrate the constructs into the locus of choice and confirmed by PCR and fluorescence microscopy (Bahler *et al*., 1998).

Either *pFA6a-(FPgene)-kanMX6* or *pFA6a-kanMX6-P(gene of interest)-mEos3.2* was used, depending on whether C-terminal or N-terminal tagging of the gene was desired, where (*FPgene*) denotes monomeric EGFP (mEGFP), mEos3.2, mCherry, or HALO. Primers with 80 base pairs of homologous sequence flanking the integration site (obtained at www.bahlerlab.info/resources/) and two repeats of GGA GGT to create a 4xGly linker were used to amplify the vector of choice. Except for the mEGFP-Lifeact construct, all tagged genes were under the control of their endogenous promoter. Strains with gene deletions were created using the *PFA6a-natMX6* vector and primers with 80 base pairs of homologous sequence flanking the region to be deleted. Cells were grown in an exponential phase for 36–48 h before imaging. To deplete the expression of Cdc15p, cells with the *Pnmt81x-cdc15* or *Pnmt81x-mCherry-cdc15* construct were grown for 24 h in yeast extract with 5 supplements (YE5S) and switched to YE5S + 15 µM thiamine for 16–18 h before imaging.

Cells expressing Cdc15p-HALO were stained with 250 nM HaloTag TMR Ligand, Cdc15p-HALO*TMR (Promega, Catalogue #G8251) for 1 h in a shaking incubator at 25°C. Cells were pelleted as described below. The supernatant was removed, and the pellet was rinsed three times with Edinburgh minimal medium with 5 supplements (EMM5S). The cells were then washed for 30–60 min with EMM5S in a shaking incubator. Cells were then pelleted and mounted for imaging as described below.

To synchronize the population of cells, we used the temperature-sensitive *cdc25-22* mutation to arrest cells at the G2-M transition at the restrictive temperature of 34°C for 4 h. We then released cells into mitosis at the permissive temperature of 22°C as a synchronized population.

Treatment with LatA to depolymerize the actin cytoskeleton during imaging was performed with either 5 or 10 µM LatA. After addition of the drug, the cells were mounted as described below and imaged immediately.

Cells used to calculate ring offset and sliding were pelleted as described below and stained with Fluorescent Brightener 28 (FB28; Sigma-Aldrich) to highlight the cell wall. FB28 was stored at –20°C in 5 mg/ml aliquots. Before use, the aliquots were thawed and briefly spun down to remove debris. Immediately before imaging, 500 µg/ml FB28 was added to the sample and mixed gently before mounting as described below. A new aliquot was used for each imaging session.

Spinning-disk confocal microscopy and data analysis

Cells were grown in an exponential phase at 25°C in YE5S-rich liquid medium in 50-ml baffled flasks in a shaking incubator in the dark. Fluorescence images of live cells were acquired with a Nikon Eclipse Ti microscope equipped with a 100×/numerical aperture (NA) 1.49 HP Apo TIRF objective (Nikon), a CSU-X1 (Yokogawa) confocal spinning-disk system, 405/488/561/647 nm solid state lasers, and an electron-multiplying cooled charge-coupled device camera (EMCCD IXon 897; Andor Technology). The Nikon Element software was used for acquisition. Cells were concentrated 10- to 20-fold by centrifugation at 2400 × *g* for 30 s and then resuspended in EMM5S. Cells (5 µl) were mounted on a thin gelatin pad consisting of 10 µl of 25% gelatin (Sigma-Aldrich; G-2500) in EMM5S, sealed under a #1.5 coverslip with VALAP (1:1:1 Vaseline:lanolin:parafin), and observed at 22°C.

ImageJ (Schneider *et al.*, 2012) and/or Nikon Element was used to create maximum or sum intensity projections of images, montages, and other image analyses. Except for time-lapse micrographs acquired after laser ablation, images in the figures are either maximum or sum intensity projections of z-sections spaced at 0.36 µm. Images were systematically contrasted to provide the best visualization, and images within the same figure panel were contrasted using the same settings. Confocal fluorescence micrographs in the figures are shown as inverted grayscale lookup tables (LUTs), except for merged color images. The ring constriction rate was measured using kymographs of maximum projection images (19 z-confocal planes taken across 6.48 µm) of time-lapse data sets taken at 1-min time intervals. The kymographs were thresholded, and the circumference was calculated automatically for each time point. These values were plotted in Microsoft Excel and the constriction rate calculated using a linear regression. Student's *t* tests were used to determine whether constriction rates differed significantly between planned comparisons of strains.

The percentage offset of the contractile ring was measured using maximum-intensity projections of single time points of cells expressing mEGFP-Myo2p and stained with FB28 to highlight the cell wall. The center of the cell was calculated as the cell length (*L*) divided by 2. The position of the contractile ring (*X*) was measured as the distance between the cell end and the contractile ring. For ring offset in still images, only rings that had septa stained with FB28 were used. The change in contractile ring offset was calculated using the following equation:

$$\text{Percentage ring offset} = \left(\frac{\left| X - (L/2) \right|}{L/2} \right) * 100$$

To calculate the percentage ring offset following sliding using time-lapse micrographs, we measured the position of the contractile ring at the time point when it was fully assembled (X_a) and the position of the contractile ring at the onset of constriction (X_c). We calculated the difference between the ring offset at both time points using the following equation:

$$\text{Percentage ring offset following sliding} = \left(\frac{\left(\left| Xc - (L/2) \right| \right) - \left(Xa - (L/2) \right)}{L/2} \right) * 100$$

To count proteins in contractile rings, we created sum projection images of fields of cells from stacks of 21 optical images separated by 0.36 µm (Wu and Pollard, 2005; Wu *et al.*, 2008). The images were corrected for camera noise and uneven illumination, and then the fluorescence intensity of contractile rings was measured. These fluorescence intensity measurements were compared against a standard curve of proteins tagged endogenously with mEGFP to determine the number of molecules per contractile ring (Wu and Pollard, 2005; Wu *et al.*, 2008). The resulting actin monomer values from strains containing the mEGFP-Lifeact construct were then scaled appropriately to reflect that this Lifeact construct marks 6% of polymerized actin (Malla *et al.*, 2022). A standard least squares model of the form *Y* = Ring Diameter + Genotype + Ring Diameter*Genotype, where *Y* is number of polypeptides, was used to determine whether the distribution of polypeptides in the constricting contractile ring differed between wild-type and either Δ*imp2* or *Pnmt81-cdc15* cells. Tests were performed with JMP Pro 16 (SAS Institute, Cary, NC).

SMLM data acquisition and display

SMLM imaging was performed with a Nikon STORM system operating in 2D mode, calibrated for single molecule acquisition in live cells. Samples were imaged with epi illumination to photoconvert and excite fluorophores. Single molecules were captured with an sCMOS camera (ORCA-Flash4.0; Hamamatsu) operating at

200 frames per second using Nikon Element software. Powers for both 405 and 561 nm lasers were optimized for distinct minimally overlapping single molecule emissions (Bellingham-Johnstun *et al.*, 2021). The average laser power density of the 561-nm laser used to excite the photoconverted mEos3.2 for imaging was ~0.3 kW/cm^2 illuminating an ~5500 μm^2 area. To maintain a density of photoconverted mEos3.2 at an appropriate level for single-molecule localizations, the power of the 405-nm laser used for photoconversion was increased manually every 5 s during data acquisition. The total power of the 405-nm laser ranged from 0 to 32 μW.

Acquired data were processed to localize single molecules as previously described (Laplante *et al.*, 2016a,b). Acquired frames were analyzed using a custom sCMOS-specific localization algorithm based on a maximum likelihood estimator (MLE) as described previously (Huang *et al.*, 2013; Laplante *et al.*, 2016a,b). A log-likelihood ratio was used as the rejection algorithm to filter out overlapping emitters, nonconverging fits, out-of-focus single molecules, and artifacts caused by rapid movements during one camera exposure time (Huang *et al.*, 2011, 2013). The accepted estimates were reconstructed in a 2D histogram image of 5-nm pixels, where the integer value in each pixel represented the number of localization estimates within that pixel. Images for visualization purposes were generated with each localization convolved with a 2D Gaussian kernel (σ = 7.5 nm). Images were reconstructed from all or a subset of acquired frames and color coded either for the temporal information (JET LUT map) or for localization density (Heat LUT map). Our localization algorithm eliminated out-of-focus emissions, providing an effective depth of field of ~400 nm (Laplante *et al.*, 2016b).

Node identification and measurements

Clusters of localized emitters associated with cytokinesis structures were manually selected from the reconstructed SMLM images. For comparison purposes, all nodes were cropped from images reconstructed from 1000 frames (5 s) to minimize blurring due to crowding and movement and allow for the selection of individual nodes.

The edge of the cell was identified by increasing the brightness of SMLM images to enhance the cytoplasmic background. The edge of the cell was located where the cytoplasmic background drops off at the interface with the space outside the cells (Laplante *et al.*, 2016b).

We analyzed ring nodes from contractile rings that had constricted by 20–50%. Ring nodes were difficult to segment if the contractile rings were constricted by more than 50% due to the density and movement of the ring nodes. All nodes were cropped using a 309 × 309 nm box in MATLAB.

Spatial and temporal information provided by each localized mEos3.2 emitter was used to measure the dimensions and stoichiometry of proteins within ring nodes. By treating each localized emitter as an independent measurement and utilizing the large number of localizations, the RDD approach becomes more robust than typical line profile measurements of fluorescence intensity.

Individual nodes were cropped, and the RDD of their single molecule emitters were plotted as previously described (Laplante *et al.*, 2016b). We reconstructed position estimates of the emitters in 2D histogram images from face views of isolated nodes obtained from the cropping step with pixel size of 2 nm to avoid pixelation errors in the subsequent measurement analysis. These images were then fitted with a rotationally symmetric 2D Gaussian model with amplitude and sigma and center position in *x* and *y* as the fitting parameters. The radial symmetry centers of each node (Parthasarathy, 2012) were determined and used as the initial guesses for the *x*, *y* center in the fitting. MLE-based regression was performed assuming a Poisson noise model of the 2D histogram image using the Nelder–Mead simplex algorithm implemented in the MATLAB "fminsearch" function. Fitting estimates were filtered by their likelihood values thereafter. Fitting results that did not converge properly and resulted in center positions outside the image boundary or extremely large or small sigma values were also discarded from the results. This step eliminates instances where two objects were included in the same 309 × 309 nm selection box and includes only selections containing a single cluster. For each node accepted through the filtering process, the distances of individual localizations from the estimated node center were calculated. All distances measured from a specific node type and view were plotted into histograms and then subsequently normalized by their radius to give a RDD. The number of localizations per identified node was recorded as well.

We used a two-sample Kolmogorov-Smirnov (KS) test to compare the distributions of localizations in each pair of node proteins. The null hypothesis is that the samples are drawn from the same distribution of localized emitters. The cumulative distribution functions (CDFs) of the squared radial distance were calculated for each of the samples (Supplemental Figure 3B), and the maximum difference between pairs of CDFs was calculated and compared with the KS test critical value at a significance level of $p < 0.005$. If the maximum difference between the CDFs was greater than the critical value, the null hypothesis was rejected. The results of the KS test comparisons and sample size of the SMLM data sets can be found in Supplemental Figure 3A.

The radius of each node marker was calculated using the CDF plots and was defined as the distance from the center of the node that contained 75% of the localized emitters (Figure 3E and Supplemental Figure 3B).

Quantification of localized emitters

For each marker and genetic background, we measured the total number of localized emitters per protein complex. The number of localized emitters per complex is influenced by many factors, including the total number of frames used for the reconstruction, the photophysics of the fluorescent proteins, the number of tagged proteins per node, and the autofluorescence background.

We used an analysis of variance with Tukey's honestly significant difference (HSD) test to compare the number of localizations per complex between genotypes at a significance level $p < 0.05$.

Laser ablation and displacement analysis

We severed constricting contractile rings in wild-type and Δ*imp2* cells expressing mEGFP-Myp2p. We focused on constricting contractile rings (~75% of their initial size, corresponding to 8–9 μm in circumference) to avoid potentially confounding results from contractile rings that have not yet started to constrict as they may have distinct mechanical properties. While we were able to visualize both severed tips in a few severed contractile rings, only one tip remained in our observation plane in most cases (Supplemental Figure 1A). We ablated 18 contractile rings in wild-type cells and 14 contractile rings in Δ*imp2* cells. This resulted in 18 severed tips that could be analyzed for the recoil phase of wild-type cells and 14 severed tips in Δ*imp2* cells.

Laser ablation was performed on a Nikon Ti-E microscope equipped with an Andor Dragonfly spinning-disk confocal fluorescence microscope equipped with a 100× NA 1.45 objective (Nikon) and a built-in 1.5× magnifier, a 488 nm diode laser with Borealis attachment (Andor), emission filter Chroma ET525/50m, and an EMCCD camera (iXon3, Andor Technology). Fusion software (Andor) was used to control data acquisition. Targeted laser ablation was performed using a MicroPoint (Andor) system with galvo-controlled

steering to deliver two sets of 15 3 ns pulses of 551 nm light at 16 Hz (Andor) mounted on the Dragonfly microscope described above, as previously described (Moshtohry *et al.*, 2022). Fusion software (Andor) was used to control acquisition while IQ software (Andor) was used simultaneously to control laser ablation. At this pulse rate, the ablation process lasts 1–2 s. A Chroma ET610LP mounted in the dichroic position of a Nikon filter turret was used to deliver the ablation laser to the sample. Because this filter also reflects the mEGFP emission, the camera frames collected during the ablation process are blank. The behavior of severed contractile rings was imaged immediately following laser ablation by acquiring a single confocal plane in the 488-nm channel every second for up to 5 min. We acquired time-lapse images of a single optical plane of the surface of the contractile ring to maximize temporal resolution and reduce photodamage. The mechanism of ablative photodecomposition remains unclear but may be caused by either the propagation of a pressure wave and/or cavitation bubble dynamics (Venugopalan *et al.*, 2002; Rau *et al.*, 2006). The size of the damage is approximately the size of the diffraction spot of the lens <0.4 µm in the *XY* plane and <0.8 in the *Z*-axis (Khodjakov *et al.*, 1997).

The displacement of the tips of severed contractile rings was tracked manually every second after laser ablation using the "multipoint" tool in FIJI on single *z*-plane time-lapse micrographs. The severed tips were tracked until they recoiled out of the imaging plane or until the contractile ring was healed. The coordinates of the tracked severed tips were exported as a CSV file. The displacement of the severed tips starting from the first frame after severing, $t = 0$ s, was calculated from the coordinates of the tracked severed tips using custom Python codes (Moshtohry *et al.*, 2022). The recoil displacement traces from each cell were aligned to $t = 0$ s, and the mean displacement curve was calculated for each genotype. The recoil displacement traces show the combined recoil phase of all severed tips exclusively. The recoil displacement of each of the severed tips contributes to the traces until the recoil halts. The mean displacement curve for each genotype was fitted to a single exponential $\Delta L(t) = A(1-e^{-\frac{t}{\tau}})$ using a least squares fit, and the SE on the least squares fit is reported. Contractile rings were considered fully ablated if there was no remaining fluorescence joining the ablated tips of the ring and the ablated ends showed evidence of recoil away from the site of ablation. Ablated rings with an individual $R^2 < 0.3$ were not included in Figure 2B due to poorness of fit.

ACKNOWLEDGMENTS

We thank Pilar Pérez and Juan Carlos Ribas for sharing materials. We thank Parsa Zareiesfandabadi, Mary Williard Elting, and Marcus Begley for technical support with laser ablation. We thank the cellular and molecular imaging facility (CMIF) at North Carolina State University (supported by the State of North Carolina and the National Science Foundation) for the ablation microscope. B.C. was supported by National Institutes of Health (NIH) T32 5T32-AI0502080-17. This work was funded by NIH R01GM134254.

REFERENCES

Arasada R, Pollard TD (2011). Distinct roles for F-BAR proteins Cdc15p and Bzz1p in actin polymerization at sites of endocytosis in fission yeast. Curr Biol 21, 1450–1459.

Arasada R, Pollard TD (2014). Contractile ring stability in S. pombe depends on F-BAR protein Cdc15p and Bgs1p transport from the Golgi complex. Cell Rep 8, 1533–1544.

Bahler J, Wu JQ, Longtine MS, Shah NG, McKenzie A 3rd, Steever AB, Wach A, Philippsen P, Pringle JR (1998). Heterologous modules for efficient and versatile PCR-based gene targeting in Schizosaccharomyces pombe. Yeast 14, 943–951.

Bellingham-Johnstun K, Anders EC, Ravi J, Bruinsma C, Laplante C (2021). Molecular organization of cytokinesis node predicts the constriction rate of the contractile ring. J Cell Biol 220, e202008032.

Bhattacharjee R, Mangione MC, Wos M, Chen JS, Snider CE, Roberts-Galbraith RH, McDonald NA, Presti LL, Martin SG, Gould KL (2020). DYRK kinase Pom1 drives F-BAR protein Cdc15 from the membrane to promote medial division. Mol Biol Cell 31, 917–929.

Bohnert KA, Gould KL (2012). Cytokinesis-based constraints on polarized cell growth in fission yeast. PLoS Genet 8, e1003004.

Carnahan RH, Gould KL (2003). The PCH family protein, Cdc15p, recruits two F-actin nucleation pathways to coordinate cytokinetic actin ring formation in Schizosaccharomyces pombe. J Cell Biol 162, 851–862.

Colombelli J, Besser A, Kress H, Reynaud EG, Girard P, Caussinus E, Haselmann U, Small JV, Schwarz US, Stelzer EH (2009). Mechanosensing in actin stress fibers revealed by a close correlation between force and protein localization. J Cell Sci 122, 1665–1679.

Cortes JC, Ishiguro J, Duran A, Ribas JC (2002). Localization of the (1,3) beta-D-glucan synthase catalytic subunit homologue Bgs1p/Cps1p from fission yeast suggests that it is involved in septation, polarized growth, mating, spore wall formation and spore germination. J Cell Sci 115, 4081–4096.

Demeter J, Sazer S (1998). imp2, a new component of the actin ring in the fission yeast Schizosaccharomyces pombe. J Cell Biol 143, 415–427.

Fankhauser C, Reymond A, Cerutti L, Utzig S, Hofmann K, Simanis V (1995). The S. pombe cdc15 gene is a key element in the reorganization of F-actin at mitosis. Cell 82, 435–444.

Huang F, Hartwich TM, Rivera-Molina FE, Lin Y, Duim WC, Long JJ, Uchil PD, Myers JR, Baird MA, Mothes W, *et al.* (2013). Video-rate nanoscopy using sCMOS camera-specific single-molecule localization algorithms. Nat Methods 10, 653–658.

Huang F, Schwartz SL, Byars JM, Lidke KA (2011). Simultaneous multiple-emitter fitting for single molecule super-resolution imaging. Biomed Opt Express 2, 1377–1393.

Khodjakov A, Cole RW, Rieder CL (1997). A synergy of technologies: combining laser microsurgery with green fluorescent protein tagging. Cell Motil Cytoskeleton 38, 311–317.

Kumar S, Maxwell IZ, Heisterkamp A, Polte TR, Lele TP, Salanga M, Mazur E, Ingber DE (2006). Viscoelastic retraction of single living stress fibers and its impact on cell shape, cytoskeletal organization, and extracellular matrix mechanics. Biophys J 90, 3762–3773.

Laplante C, Berro J, Karatekin E, Hernandez-Leyva A, Lee R, Pollard TD (2015). Three myosins contribute uniquely to the assembly and constriction of the fission yeast cytokinetic contractile ring. Curr Biol 25, 1955–1965.

Laplante C, Huang F, Bewersdorf J, Pollard TD (2016a). High-speed super-resolution imaging of live fission yeast cells. Methods Mol Biol 1369, 45–57.

Laplante C, Huang F, Tebbs IR, Bewersdorf J, Pollard TD (2016b). Molecular organization of cytokinesis nodes and contractile rings by super-resolution fluorescence microscopy of live fission yeast. Proc Natl Acad Sci USA 113, E5876–E5885.

Laporte D, Coffman VC, Lee IJ, Wu JQ (2011). Assembly and architecture of precursor nodes during fission yeast cytokinesis. J Cell Biol 192, 1005–1021.

Lee ME, Rusin SF, Jenkins N, Kettenbach AN, Moseley JB (2018). Mechanisms connecting the conserved protein kinases Ssp1, Kin1, and Pom1 in fission yeast cell polarity and division. Curr Biol 28, 84–92.e84.

Magliozzi JO, Sears J, Cressey L, Brady M, Opalko HE, Kettenbach AN, Moseley JB (2020). Fission yeast Pak1 phosphorylates anillin-like Mid1 for spatial control of cytokinesis. J Cell Biol 219, e201908017.

Malla M, Pollard TD, Chen Q (2022). Counting actin in contractile rings reveals novel contributions of cofilin and type II myosins to fission yeast cytokinesis. Mol Biol Cell 33, ar51.

Mangione MC, Snider CE, Gould KL (2019). The intrinsically disordered region of the cytokinetic F-BAR protein Cdc15 performs a unique essential function in maintenance of cytokinetic ring integrity. Mol Biol Cell 30, 2790–2801.

Martin-Garcia R, Coll PM, Perez P (2014). F-BAR domain protein Rga7 collaborates with Cdc15 and Imp2 to ensure proper cytokinesis in fission yeast. J Cell Sci 127, 4146–4158.

Martin-Garcia R, Valdivieso MH (2006). The fission yeast Chs2 protein interacts with the type-II myosin Myo3p and is required for the integrity of the actomyosin ring. J Cell Sci 119, 2768–2779.

McDargh Z, Wang S, Chin HF, Thiyagarajan S, Karatekin E, Pollard TD, O'Shaughnessy B (2021). Myosins generate contractile force and

maintain organization in the cytokinetic contractile ring. bioRxiv https://doi.org/10.1101/2021.05.02.442363.
McDonald NA, Lind AL, Smith SE, Li R, Gould KL (2017). Nanoscale architecture of the Schizosaccharomyces pombe contractile ring. eLife 6, e28865.
McDonald NA, Takizawa Y, Feoktistova A, Xu P, Ohi MD, Vander Kooi CW, Gould KL (2016). The tubulation activity of a fission yeast F-BAR protein is dispensable for its function in cytokinesis. Cell Rep 14, 534–546.
McDonald NA, Vander Kooi CW, Ohi MD, Gould KL (2015). Oligomerization but not membrane bending underlies the function of certain F-BAR proteins in cell motility and cytokinesis. Dev Cell 35, 725–736.
Moseley JB, Mayeux A, Paoletti A, Nurse P (2009). A spatial gradient coordinates cell size and mitotic entry in fission yeast. Nature 459, 857–860.
Moshtohry M, Bellingham-Johnstun K, Elting MW, Laplante C (2022). Laser ablation reveals the impact of Cdc15p on the stiffness of the contractile ring. Mol Biol Cell 33, br9.
Parthasarathy R (2012). Rapid, accurate particle tracking by calculation of radial symmetry centers. Nat Methods 9, 724–726.
Rau KR, Quinto-Su PA, Hellman AN, Venugopalan V (2006). Pulsed laser microbeam-induced cell lysis: time-resolved imaging and analysis of hydrodynamic effects. Biophys J 91, 317–329.
Ren L, Willet AH, Roberts-Galbraith RH, McDonald NA, Feoktistova A, Chen JS, Huang H, Guillen R, Boone C, Sidhu SS, *et al.* (2015). The Cdc15 and Imp2 SH3 domains cooperatively scaffold a network of proteins that redundantly ensure efficient cell division in fission yeast. Mol Biol Cell 26, 256–269.
Roberts-Galbraith RH, Chen JS, Wang J, Gould KL (2009). The SH3 domains of two PCH family members cooperate in assembly of the Schizosaccharomyces pombe contractile ring. J Cell Biol 184, 113–127.
Roberts-Galbraith RH, Ohi MD, Ballif BA, Chen JS, McLeod I, McDonald WH, Gygi SP, Yates JR 3rd, Gould KL (2010). Dephosphorylation of F-BAR protein Cdc15 modulates its conformation and stimulates its scaffolding activity at the cell division site. Mol Cell 39, 86–99.
Roca-Cusachs P, Conte V, Trepat X (2017). Quantifying forces in cell biology. Nat Cell Biol 19, 742–751.
Schneider CA, Rasband WS, Eliceiri KW (2012). NIH Image to ImageJ: 25 years of image analysis. Nat Methods 9, 671–675.
Sethi K, Palani S, Cortes JC, Sato M, Sevugan M, Ramos M, Vijaykumar S, Osumi M, Naqvi NI, Ribas JC, Balasubramanian M (2016). A new membrane protein Sbg1 links the contractile ring apparatus and septum synthesis machinery in fission yeast. PLoS Genet 12, e1006383.
Silva AM, Osorio DS, Pereira AJ, Maiato H, Pinto IM, Rubinstein B, Gassmann R, Telley IA, Carvalho AX (2016). Robust gap repair in the contractile ring ensures timely completion of cytokinesis. J Cell Biol 215, 789–799.
Snider CE, Chandra M, McDonald NA, Willet AH, Collier SE, Ohi MD, Jackson LP, Gould KL (2020). Opposite surfaces of the Cdc15 F-BAR domain create a membrane platform that coordinates cytoskeletal and signaling components for cytokinesis. Cell Rep 33, 108526.
Snider CE, Willet AH, Chen JS, Arpag G, Zanic M, Gould KL (2017). Phosphoinositide-mediated ring anchoring resists perpendicular forces to promote medial cytokinesis. J Cell Biol 216, 3041–3050.
Vavylonis D, Wu JQ, Hao S, O'Shaughnessy B, Pollard TD (2008). Assembly mechanism of the contractile ring for cytokinesis by fission yeast. Science 319, 97–100.
Venugopalan V, Guerra A 3rd, Nahen K, Vogel A (2002). Role of laser-induced plasma formation in pulsed cellular microsurgery and micromanipulation. Phys Rev Lett 88, 078103.
Willet AH, Bohnert KA, Gould KL (2018). Cdk1-dependent phosphoinhibition of a formin-F-BAR interaction opposes cytokinetic contractile ring formation. Mol Biol Cell 29, 713–721.
Willet AH, Igarashi MG, Chen JS, Bhattacharjee R, Ren L, Cullati SN, Elmore ZC, Roberts-Galbraith RH, Johnson AE, Beckley JR, Gould KL (2021). Phosphorylation in the intrinsically disordered region of F-BAR protein Imp2 regulates its contractile ring recruitment. J Cell Sci 134, jcs258645.
Willet AH, McDonald NA, Bohnert KA, Baird MA, Allen JR, Davidson MW, Gould KL (2015). The F-BAR Cdc15 promotes contractile ring formation through the direct recruitment of the formin Cdc12. J Cell Biol 208, 391–399.
Wu JQ, Kuhn JR, Kovar DR, Pollard TD (2003). Spatial and temporal pathway for assembly and constriction of the contractile ring in fission yeast cytokinesis. Dev Cell 5, 723–734.
Wu JQ, McCormick CD, Pollard TD (2008). Chapter 9: Counting proteins in living cells by quantitative fluorescence microscopy with internal standards. Methods Cell Biol 89, 253–273.
Wu JQ, Pollard TD (2005). Counting cytokinesis proteins globally and locally in fission yeast. Science 310, 310–314.
Wu JQ, Sirotkin V, Kovar DR, Lord M, Beltzner CC, Kuhn JR, Pollard TD (2006). Assembly of the cytokinetic contractile ring from a broad band of nodes in fission yeast. J Cell Biol 174, 391–402.